

Surface plasmon mediated transmission of subwavelength slits at THz frequencies

T. H. Isaac,¹ J. Gómez Rivas,² J. R. Sambles,¹ W. L. Barnes,¹ and E. Hendry¹

¹*School of Physics, University of Exeter, Stocker Road, Exeter EX4 4QL, United Kingdom*

²*FOM Institute for Atomic and Molecular Physics, Kruislaan 407, 1098 SJ Amsterdam, The Netherlands*

(Received 22 December 2007; revised manuscript received 19 February 2008; published 28 March 2008)

We present measurements and a numerical modeling that elucidate the role of surface plasmons in the resonant transmission of a subwavelength slit in a conducting material. By using THz time domain spectroscopy, we determine the Fabry–Pérot transmission resonances for a single slit formed from a wafer of a semiconductor with a surface plasma frequency in the THz frequency range. We measure large redshifts in the resonant frequencies close to the surface plasma frequency, which are 50% lower than the resonance frequencies expected well below the surface plasma frequency. This is an effect attributed to the coupling of plasmons on the adjacent surfaces of the slit.

DOI: [10.1103/PhysRevB.77.113411](https://doi.org/10.1103/PhysRevB.77.113411)

PACS number(s): 73.20.Mf, 42.79.Ag, 71.45.Gm, 78.20.Ci

The resonant transmission of radiation through a subwavelength slit in a screen of a conducting material has recently been the subject of considerable theoretical^{1–5} and experimental^{6–8} work. For some time, it has been known that narrow slits in metals at low frequencies support Fabry–Pérot (FP) resonances, where an approximately half-integer number of wavelengths are quantized along the length of the slit. These quantized modes give rise to transmission resonances⁹ of frequency ν_{FP} given by

$$\nu_{\text{FP}} = \frac{nc}{2l}, \quad (1)$$

where l is the length of the slit and n is an integer. For a slit in a slab of a perfect metal (a material with infinite conductivity at all frequencies), it has been shown that Eq. (1) provides an accurate estimate of the resonant transmission frequencies, provided that the slits are very narrow compared to the wavelength of the transmitted radiation.^{3,10}

However, for the case of narrow slits in real conductors with finite conductivity, the modes within the slits are coupled surface plasmons (SPs), and one obtains very large redshifts^{1,2} from the resonant transmission frequencies predicted by Eq. (1). Resonant slit cavities are featured in many photonic structures, many of which have potential applications in sensing or spectroscopy.^{5,11,12} It is, therefore, important to understand the role of SPs in influencing the resonant behavior of this fundamental system.

Here, we present measurements and a numerical modeling that elucidate the role of SPs in the transmission of subwavelength slits in conducting materials. By using THz time domain spectroscopy (THz-TDS), we determine the behavior of FP transmission resonances for slits formed in wafers of indium antimonide (InSb), which has a surface plasma frequency (ω_{SP}) of approximately 1.7 THz (10.7×10^{12} rad/s). For narrow slits in the InSb, we find that near the surface plasma frequency, resonances are redshifted by more than 50% from the values predicted by Eq. (1). This frequency shift is more than 2 orders of magnitude larger than the shifts reported in metals at low frequencies.⁹ By measuring the phase delay of the transmitted radiation, we demonstrate that the coupling of SPs on the surfaces within the slit modifies

the effective index of the mode within the cavity and, hence, the frequency of resonant transmission. This effect becomes significantly stronger for frequencies approaching the surface plasma frequency.

Semiconductors have remarkably tunable dielectric functions. We choose a semiconductor with a surface plasma frequency in the THz range, so that the THz dielectric function is similar to that of metals at visible-ultraviolet frequencies. The dielectric function $\epsilon(\omega)$ of InSb in this frequency region can be approximated by using the Drude model,

$$\epsilon(\omega) = \epsilon_{\text{lattice}} - \frac{\omega_p^2}{\omega^2 + i\omega\gamma}. \quad (2)$$

In this model, $\epsilon_{\text{lattice}}$ is the zero frequency permittivity of the semiconductor, ω_p is the plasma frequency of the conductor, and γ is the scattering frequency. In Fig. 1(a), we plot the room temperature dielectric function for typical InSb wafers by using Drude parameters from the literature,¹³ with $\gamma \approx 0.8 \times 10^{12}$ rad/s and $\omega_p \approx 40 \times 10^{12}$ rad/s. Below, we will refine the values of the Drude parameters for the samples of InSb used in our measurements.

Figure 1(a) shows the large change in the dielectric function of InSb across the THz frequency range. The surface plasma frequency for a conductor-air interface is defined¹⁴ as the frequency at which $\epsilon_{\text{real}} = -1$ and represents the high-frequency cutoff for a SP mode propagating on that interface.¹⁵ The imaginary component of the dielectric function for InSb, which determines loss, is relatively small in this frequency range. In order to obtain ω_{SP} in the THz frequency range, other common semiconductors must be heavily doped. For example, to obtain $\omega_{\text{SP}} = 2.0$ THz for n -doped GaAs,¹⁶ $\omega_p = 45 \times 10^{12}$ rad/s and $\gamma = 3.9 \times 10^{12}$ rad/s. Similarly, for n -doped silicon¹⁷ with $\omega_{\text{SP}} = 0.7$ THz, the Drude parameters are $\omega_p = 17 \times 10^{12}$ rad/s and $\gamma = 5.2 \times 10^{12}$ rad/s. In general, higher scattering rates will lead to SPs with shorter propagation lengths for a given surface plasma frequency.

The sample under investigation consists of a slit aperture in a wafer of undoped InSb with a DC conductivity at 77 K of approximately 2400 S m^{-1} and a thickness of $456 \text{ }\mu\text{m}$. The aperture is formed by cleaving a monocrystalline wafer

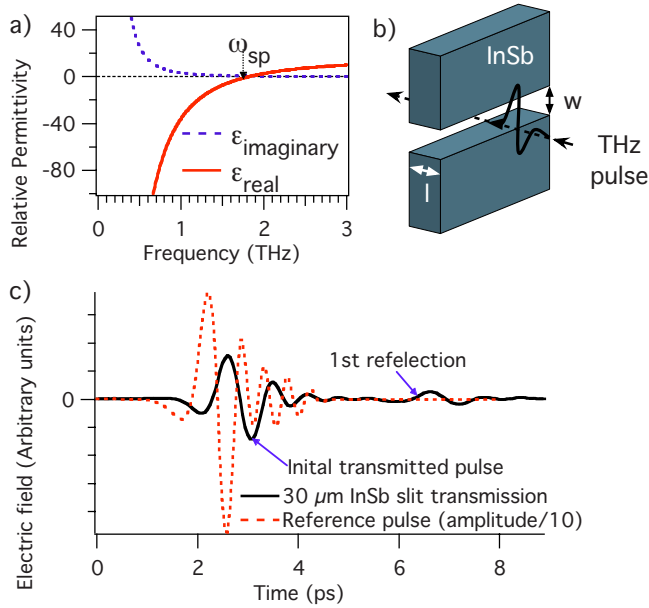


FIG. 1. (Color online) (a) Drude modeled permittivity of InSb. ω_{SP} (for which $\epsilon_{\text{real}} = -1$) is indicated. (b) Transmission of a THz pulse through an aperture defined by mechanically variable width w and fixed length l . (c) Time domain electric field of a THz pulse measured in the far field after transmission through a $30 \mu\text{m}$ wide aperture; the reflected pulse, which has made one round trip of the slit length l , is indicated. Also shown is the reference pulse, with the amplitude scaled down by a factor of 10.

of InSb along a crystal plane using a diamond scribe. The two interfaces are aligned parallel to each other under a microscope mounted onto micrometer translation stages so that the width w of the slit is variable and is placed near the focus of a conical beam in a THz spectrometer. The resulting slit is defined by length l and width w [see Fig. 1(b)]. Under an optical microscope, the sides of the slit are observed to be flat to within a few microns across its length.

The transmission of the slits is measured with incident THz radiation polarized normal to the slit. In general, the polarization of the incident radiation must be TM with respect to the planes of top and bottom slit interfaces in order to excite SPs within the slit and observe resonant transmission; there are, however, some special cases in which TE modes can be supported within a subwavelength slit through the inclusion of a high index dielectric material inside the cavity.¹⁸ Here, we only consider the case of air-filled slits with incident radiation polarized normal to the slit direction. All the slit sizes used are too small to support any TE cavity modes.

THz-TDS enables us to map out the electric field of a single-cycle THz pulse as a function of time by using a spectrometer similar to that reported in Ref. 19. Briefly, THz pulses are generated through optical rectification²⁰ of 800 nm, 50 fs laser pulses in a 1 mm thick $\langle 110 \rangle$ -oriented zinc telluride crystal, which results in a THz pulse with bandwidth of 0.1–3 THz. Detection is accomplished by using a second identical ZnTe crystal by means of electro-optic sampling with the 800 nm laser pulses. The resulting time domain electric field profile [such as that plotted in Fig. 1(c)]

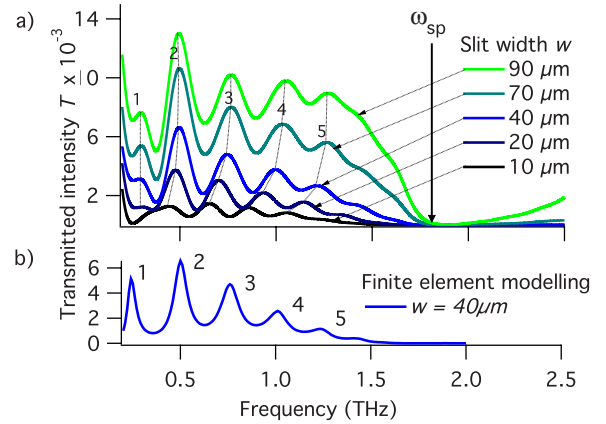


FIG. 2. (Color online) (a) Measured normalized transmission intensities for a slit in InSb for varying slit widths w of 10–90 μm . Numbered peaks label the order of the corresponding FP-like transmission. (b) Example of a finite-element-modeled (Ref. 21) spectrum through an InSb slit at $w = 40 \mu\text{m}$.

can be converted to the frequency domain by means of a fast Fourier transform, yielding the complex electric field as a function of frequency, $E(\omega) = Ae^{i\phi}$. Because the measurements are fully time resolved, it is possible to extract both the amplitude A and the phase ϕ of each frequency component. Normalized transmission intensities are found by dividing the spectral intensity transmitted through the sample by a free-space reference intensity, i.e., $T(\omega) = (A_{\text{trans}})^2 / (A_{\text{ref}})^2$. We also calculate the effective refractive index of the slit by using the phase shift between reference and sample spectra ($\Delta\phi = \phi_{\text{trans}} - \phi_{\text{ref}}$) through the relation $n_{\text{effective}} = n_0 + \Delta\phi c / \omega l$, where n_0 is the index of the reference medium (in this case air, $n_0 = 1$) and l is the length of the slit.

Time domain transmission through a slit in InSb is shown in Fig. 1(c). We first observe an initial THz pulse that is directly transmitted through the slit, followed by a smaller time-delayed pulse—this is a reflected pulse that has made one round trip of the slit. In Fig. 2(a), we plot the normalized intensity transmission spectrum as a function of frequency. The numbered transmission peaks in these figures indicate quantized FP peaks that result from cavity reflections. It should be noted that the first mode is at the very limit of the lowest measurable frequency for the THz spectrometer and, as such, has a higher level of experimental error. Note that the observed peaks considerably shift from values predicted by Eq. (1). The first five FP modes are clearly observed, and the higher order peaks are seen to broaden and decrease in amplitude as they approach the surface plasma frequency. Measured transmission spectra agree well with those obtained from finite-element modeling²¹ of the system. An example of the modeled spectra is shown in Fig. 2(b). To obtain the best agreement between measurements and the model, we vary the InSb Drude parameters. The best fit is obtained with $\omega_p = 46 \times 10^{12}$ rad/s and scattering frequency $\gamma = 0.63 \times 10^{12}$ rad/s. We take the lattice permittivity $\epsilon_{\text{lattice}}$ to be²² 15.7. These values are comparable to published values^{13,22} of InSb Drude parameters. Any small deviation among reported values is readily accounted for by the variation in impurity density between InSb samples.

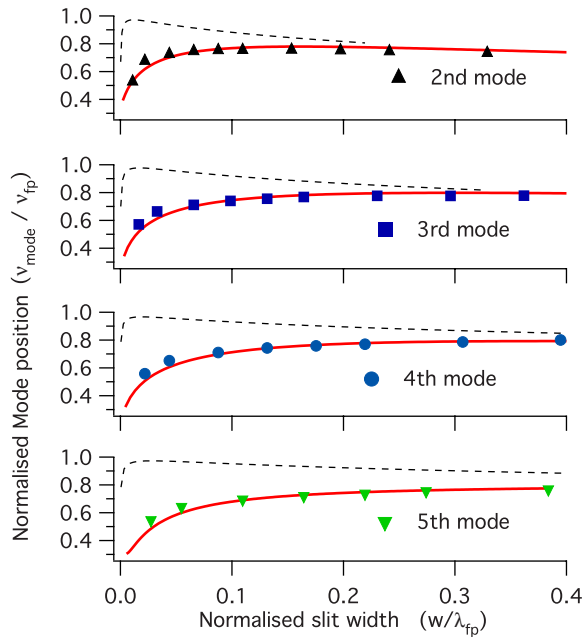


FIG. 3. (Color online) Plot of normalized resonance frequencies $\nu_{\text{mode}}/\nu_{\text{FP}}$, against normalized slit widths w/λ_{FP} for modes 2–5 in an InSb slit. The solid lines are the results of finite-element modeling, the markers are the results of measurements. The dashed lines represent the results of finite-element modeling of a slit with the same dimensions formed in aluminum.

On changing the width of the InSb slit aperture, it is clear from the transmission spectra in Fig. 2(a) that the resonance peaks shift to lower frequencies as the aperture width is decreased. In order to show the degree to which the frequency of each resonance moves, we plot the position of each resonance peak as a function of slit aperture size in Fig. 3. The frequency of the peak position (ν_{mode}) is normalized to the corresponding FP frequency given by Eq. (1). We plot $\nu_{\text{mode}}/\nu_{\text{FP}}$. The slit width is scaled by the FP transmission wavelength ($w_{\text{slit}}/\lambda_{\text{FP}}$), giving a fully normalized plot that shows the fractional change in resonant frequency against the width of the slit compared to the resonance wavelength. Figure 3 shows that the frequency of all the transmission resonances decreases for the smallest slit widths, with measurements indicating shifts of around 50% from the frequencies predicted by Eq. (1) for slits of $w/\lambda_{\text{FP}} \leq 0.02$. The plot also illustrates a change in behavior between modes dependent on their proximity to the surface plasma frequency. Higher order modes, with resonances closer to ω_{SP} , drop in frequency for slit widths that are a much larger fraction of the resonance wavelength. For example, the second order mode starts to decrease in frequency for normalized slit widths of $w/\lambda_{\text{FP}} < 0.16$, whereas the fifth order mode drops in frequency for slits of $w/\lambda_{\text{FP}} < 0.4$.

For the transmission of a slit in a conducting material, there are two effects that give rise to shifts in the resonant frequencies from those predicted by Eq. (1). First, it is known that the boundary conditions at the slit entrance and exit lead to a phase shift between light propagating inside the slit and the free-space radiation on either side of it—an analytical formulation is given by Ref. 10. This effect, which is

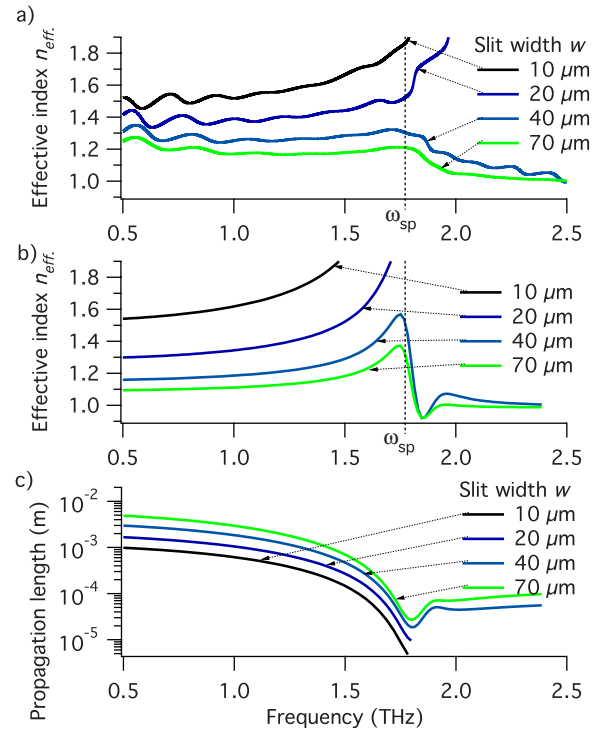


FIG. 4. (Color online) (a) The measured effective index of InSb slits with aperture widths w of 10–70 μm . The effective index of the 10 and 20 μm slits rapidly increases, approaching the surface plasma frequency. (b) Theoretically calculated values of the effective index of InSb slits of varying widths w . (c) The calculated propagation length of the coupled SP inside the InSb slits for various slit widths w .

important even for slits in highly conducting materials (i.e., those materials with surface plasma frequencies considerably higher than the frequency of the incident light), results in decreasing resonance frequencies for increasing slit widths.^{9,10} This effect explains why $\nu_{\text{mode}}/\nu_{\text{FP}}$ does not tend toward 1 for large slits in Fig. 3. A second effect arises from coupling of SPs on the internal interfaces of the slit,^{1,2,23} which gives rise to an increase in effective index for the cavity mode, and, therefore, to a decrease in resonance frequency for decreasing slit widths. Approximate analytical expressions for this effect (which are valid in the case of $w \ll \lambda$) are given by Refs. 23 and 24. It is clear from Fig. 3 that the coupling of SPs has a pronounced effect on $\nu_{\text{mode}}/\nu_{\text{FP}}$ for narrow slits.

Utilizing the phase-shift information $\Delta\phi$ of our measured THz spectra, we can plot the effective index for InSb slits in Fig. 4(a) by using the methods described above. First, for all the traces in Fig. 4(a), we observe some small peaks in the effective index, which correspond to peaks in the transmission spectrum [Fig. 2(a)]. These are due to the interference on the resonance of directly transmitted light and light that has made at least one round trip of the slit cavity. More significantly, there is a large change in the effective index near the surface plasma frequency. For smaller slit widths ($w \leq 20 \mu\text{m}$), the effective index appears asymptotic to the surface plasma frequency. This behavior can be seen in the effective index plots for 10 and 20 μm slits that are shown

in Fig. 4(a). For very small slits ($d \leq 20 \mu\text{m}$), the transmitted intensity above the surface plasma frequency is very small, such that our phase measurements above ω_{SP} are erroneous. For larger slit widths ($w \geq 40 \mu\text{m}$), the effective index returns to unity above the plasma frequency due to a small intensity of nonresonant transmission.

The transmission through a conducting slit in the limit of very narrow widths is mediated by coupled SPs on the opposite sides of a conductor-insulator-conductor structure.^{24,25} The complex propagation constant and, therefore, the effective index of refraction and the attenuation length of this mode can be analytically calculated. The results of these calculations are plotted as a function of frequency in Figs. 4(b) and 4(c) for different widths of the slit. Similar to the measurements [Fig. 4(a)], the effective refractive index increases as the width of the slit is reduced and as the surface plasma frequency is approached from the low frequency side. This increase is due to a greater penetration of the electromagnetic field into the conductor, which also causes the concomitant reduction in SP propagation length due to Ohmic losses. Although the agreement between the experiment and the analytic model is not perfect (owing to defects inside the slit generated by sample machining, which “smear out” the measured phase change), the calculations in Figs. 4(b) and 4(c) fully explain the general behavior of the FP resonances when approaching the surface plasma frequency—the rapid change in effective index accounts for the shift in peak position, while the change in propagation length accounts for the broadening of the resonance peaks.

The coupling of SPs has been shown to play a role in determining the transmission of a conducting slit aperture even for frequencies well below the surface plasma frequency of the slit material (e.g., aluminum at microwave

frequencies⁹). For metals, surface plasma frequencies are typically in the UV region of the spectrum.²² Using finite-element modeling, we compare the behavior of resonant transmission through our InSb slit to the behavior of an aluminum slit of the same dimensions across the same frequency range. The normalized resonance peak positions from this modeling are plotted as dashed lines in Fig. 3. The traces show that the position of each resonance in aluminum slits redshifts for very narrow slit widths. However, the shift in aluminum resonances occurs for much narrower slit widths than for the slits in InSb. Typically, the frequency drop is present in aluminum slits for $w/\lambda_{\text{FP}} \leq 0.01$. These results can be compared to the measurements on the InSb slit, in which the fifth mode redshifts for $w/\lambda_{\text{FP}} \leq 0.4$. This comparison emphasizes that near the surface plasma frequency of the slit material, resonance shifts due to coupling of SP modes occur for slits *more than two orders of magnitude larger* than the equivalent slits in highly conducting materials.

In conclusion, we have elucidated the effect of coupled surface plasmons on the FP-like transmission of THz radiation through slits in conductors. For narrow slits, we demonstrate that very large redshifts in the resonant FP frequencies may be expected near the surface plasma frequency. This is an effect that is attributed to the coupling of surface plasmons on the adjacent interfaces of the slit. These shifts must be accounted for in the design of devices that make use of resonant slit cavities, especially those with resonances close to the surface plasma frequency of the conductor.

T.H.I., J.R.S., W.L.B., and E.H. acknowledge the support from the EPSRC (U.K.). The contribution of J.G.R. is part of the research program of the “Stichting voor Fundamenteel Onderzoek der Materie”, which is financially supported by N.W.O.

- ¹J. A. Porto, F. J. García-Vidal, and J. B. Pendry, *Phys. Rev. Lett.* **83**, 2845 (1999).
- ²R. Gordon, *Phys. Rev. B* **73**, 153405 (2006).
- ³Y. Takakura, *Phys. Rev. Lett.* **86**, 5601 (2001).
- ⁴R. Parthasarathy, A. Bykhovski, B. Gelmont, T. Globus, N. Swami, and D. Woolard, *Phys. Rev. Lett.* **98**, 153906 (2007).
- ⁵J. Bravo-Abad, L. Martín-Moreno, and F. J. García-Vidal, *Phys. Rev. E* **69**, 026601 (2004).
- ⁶F. J. García-Vidal, H. J. Lezec, T. W. Ebbesen, and L. Martín-Moreno, *Phys. Rev. Lett.* **90**, 213901 (2003).
- ⁷Z. Sun, Y. S. Jung, and H. K. Kim, *Appl. Phys. Lett.* **83**, 3021 (2003).
- ⁸J. W. Lee, M. A. Seo, D. S. Kim, S. C. Jeoung, Ch. Lienau, J. H. Kang, and Q.-H. Park, *Appl. Phys. Lett.* **88**, 071114 (2006).
- ⁹J. R. Suckling, A. P. Hibbins, M. J. Lockyear, T. W. Preist, J. R. Sambles, and C. R. Lawrence, *Phys. Rev. Lett.* **92**, 147401 (2004).
- ¹⁰R. Harrington and D. Auckland, *IEEE Trans. Antennas Propag.* **28**, 616 (1980).
- ¹¹D. Crouse and P. Keshavareddy, *Opt. Express* **13**, 7760 (2005).
- ¹²Y. S. Jung, Z. Sun, J. Wuenschell, H. K. Kim, P. Kaur, L. Wang, and D. Waldeck, *Appl. Phys. Lett.* **88**, 243105 (2006).
- ¹³S. C. Howells and L. A. Schlie, *Appl. Phys. Lett.* **69**, 550 (1996).
- ¹⁴H. Raether, *Surface Plasmons on Smooth and Rough Surfaces and on Gratings* (Springer-Verlag, Berlin, 1988).
- ¹⁵F. Yang, J. R. Sambles, and G. W. Bradberry, *Phys. Rev. B* **44**, 5855 (1991).
- ¹⁶P. G. Huggard, J. A. Cluff, G. P. Moore, C. J. Shaw, S. R. Andrews, S. R. Keiding, E. H. Linfield, and D. A. Ritchie, *J. Appl. Phys.* **87**, 2382 (2000).
- ¹⁷T.-I. Jeon and D. Grischkowsky, *Phys. Rev. Lett.* **78**, 1106 (1997).
- ¹⁸D. Crouse and P. Keshavareddy, *Opt. Express* **15**, 1415 (2007).
- ¹⁹A. Nahata, A. S. Weling, and T. F. Heinz, *Appl. Phys. Lett.* **69**, 2321 (1996).
- ²⁰M. Bass, P. A. Franken, J. F. Ward, and G. Weinreich, *Phys. Rev. Lett.* **9**, 446 (1962).
- ²¹*HFSS Version 10* (Ansoft Corporation, Pittsburgh, 2006).
- ²²*Handbook of Optical Constants of Solids*, edited by E. D. Palik (Academic, New York, 1985).
- ²³S. Collin, F. Pardo, and J.-L. Pelouard, *Opt. Express* **15**, 4310 (2007).
- ²⁴S. I. Bozhevolnyi and T. Søndergaard, *Opt. Express* **15**, 10869 (2007).
- ²⁵E. N. Economou, *Phys. Rev.* **182**, 539 (1969).